Flow Visualization for Plume-Surface Interaction at Martian-relevant Lander Environments

Neil S. Rodrigues[1] and Olivia K. Tyrrell[2]
NASA Langley Research Center, Hampton, VA, 23681, USA

Chad J. Eberhart[3] and Kristopher J. McDougal[4]
NASA Marshall Space Flight Center, Huntsville, AL, 35808, USA

Ashley M. Korzun[5] and Paul M. Danehy[6]
NASA Langley Research Center, Hampton, VA, 23681, USA

This paper describes a jet impingement experiment performed in a large-scale vacuum chamber at Martian-relevant ambient pressure conditions, with the motivation of studying plume-surface interaction (PSI) caused by the exhaust plume of a lander interacting with the planetary surface. Flow visualization of an inert supersonic jet was performed using planar laser-induced fluorescence (PLIF), which is a molecular-based, two-dimensional measurement technique. Representative instantaneous and time-averaged visualizations of the impinging jet at two different nozzle flow conditions corresponding to the underexpanded and overexpanded jet regimes are presented for up to six different dimensionless altitudes h/D_e. The time-averaged measured spatial distribution of impingement pressures at these conditions is also reported. The PLIF visualizations appear to be critical towards explaining unexpected behavior in the impingement pressure, such as a higher impingement pressure for the underexpanded condition at $h/D_e = 10$, compared to a lower altitude of $h/D_e = 8$. This behavior can be attributed to differences in the stagnation shock structure observed in the PLIF images. The PLIF images also reveal significant flow separation at the nozzle exit for the overexpanded jet conditions. Further analysis of the test data as well as combined flow visualization and surface diagnostics for future ground tests will help inform engineering designs for landings on the Martian surface while mitigating PSI risks.

I. Introduction

Interactions between rocket exhaust plumes and the unimproved (i.e., no landing pad) surface during powered descent and landing of spacecraft on planetary bodies such as Mars may pose significant risks to the vehicle, landing site, nearby infrastructure, and personnel. Understanding the underlying plume-surface interaction (PSI) phenomena through ground test data can provide critical insights on the sensitivities of relevant gas and granular physics to parameters such as the spacecraft thrust, altitude, and ambient environment. Flow visualization results from a scaled ground test recently conducted within a 20-ft vacuum chamber environment at NASA Marshall Space Flight Center

[1] Optical Physicist, Advanced Measurements and Data Systems Branch, AIAA Member.
[2] Measurement Systems Research Engineer, Advanced Measurements and Data Systems Branch, AIAA Member.
[3] Aerospace Engineer, Propulsion Systems Fluid Dynamics Branch.
[4] Aerospace Engineer, Propulsion Systems Fluid Dynamics Branch.
[5] Technical Lead for SRP and PSI, Atmospheric Flight and Entry Systems Branch, AIAA Associate Fellow
[6] Senior Technologist, Advanced Measurements and Data Systems Branch, AIAA Associate Fellow.

are presented in this paper for Martian-relevant ambient pressure conditions of approximately $P_a \sim 600$ Pa. An earlier ground test performed at an adjacent 15-ft vacuum chamber used several different regolith simulants for the purposes of characterizing erosion behavior and ejecta phenomena at both lunar-relevant and Martian-relevant ambient pressure conditions.[1-4] The ground test at the 20-ft vacuum chamber focused on the induced flowfield by considering the impingement of a supersonic jet upon a flat plate at both lunar-relevant and Martian-relevant ambient pressure conditions. Flow visualization was performed using planar laser-induced fluorescence (PLIF), which is a molecular-based, planar, 2D (two-dimensional) measurement technique that can be used to visualize the flow of a targeted atom or molecule.[5] The PLIF variant performed for this test used nitric oxide (NO), which was seeded into the inert nitrogen test fluid well upstream of the test article.

In the present paper, we build upon two recent publications by Rodrigues *et al.*[6] and Tyrrell *et al.*[7], with the current focus being on examining the plume-surface interaction at Martian-relevant ambient pressure conditions. The earlier paper by Rodrigues *et al.* provided a broad overview on the entire test campaign at the 20-ft vacuum chamber facility, summarized the complex experimental systems, and highlighted two test cases each for lunar-relevant and Martian-relevant plume-surface interaction. The recent paper by Tyrrell *et al.* considered the impact of plume surface interaction experimental design choices, namely a half-space vs. a full-space design, on the plume impingement flowfield. In the present work, we focus on the Martian-relevant environment and present flow visualization data at two different nozzle flow conditions and up to six different nozzle altitudes relative to the flat impingement plate. The current work has some similarities to the plume impingement studies performed by Inman *et al.*[8-9], which were primarily designed to mitigate spacecraft damage during planetary entry. As a result, greater distances between the impingement target (e.g. spacecraft wing) and the nozzle were targeted in the previous work, compared to the current lander application that focuses on smaller distances between the supersonic nozzle and the impingement target (landing surface), representing the final descent of a lander.

II. Experimental Systems

The experiment discussed in this paper was performed inside a 20-ft diameter vacuum chamber as part of a larger test campaign, which was primarily focused on lunar-relevant lander environments. For the sub-set of results presented in this paper, an ambient pressure of approximately 600 Pa was used to simulate the Martian environment. However, air was used as the environment gas rather than a true Martian atmosphere, which primarily consists of CO_2. A CAD schematic of the vacuum chamber with the test article and primary components of the PLIF diagnostics is shown in Fig. 1.

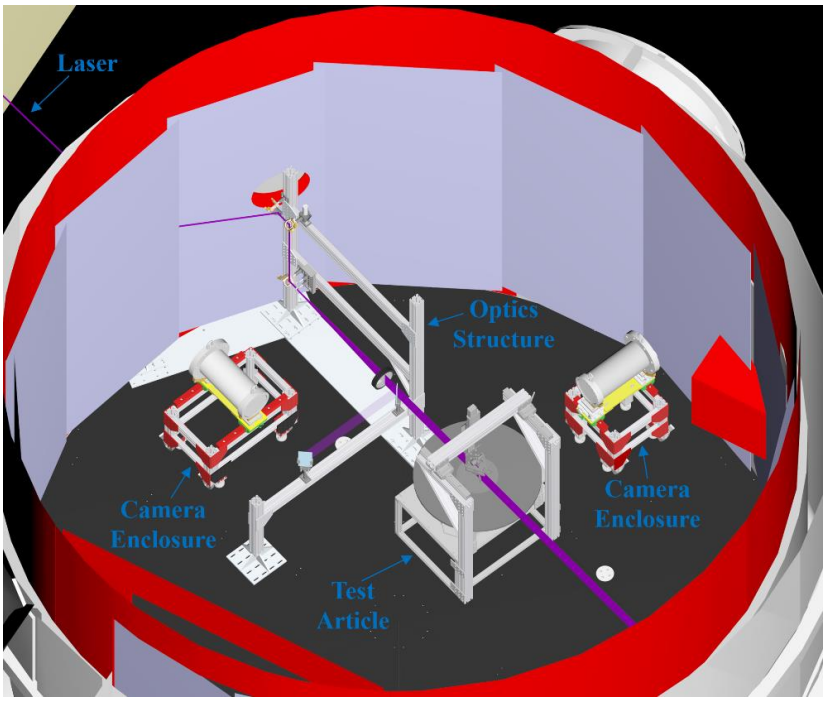

Fig. 1 CAD schematic of the vacuum chamber with the test article and PLIF instrumentation.

The test article primarily consisted of a supersonic nozzle assembly and an impingement plate assembly, which was oriented perpendicular to the nozzle flow. Both assemblies have been discussed in detail in a previous publication by Rodrigues *et al.*[6] and only a brief description of each are provided here. The supersonic nozzle features an area ratio $A/A^* = 31.7$ and an exit diameter $D_e = 1.38$ cm. Heated nitrogen premixed with nitric oxide was used as the test gas. The exit Mach number based on the area ratio and the specific heat ratio of the test gas was approximately 5.3. The nozzle assembly was installed on a vertical translation stage, which allowed the distance of the nozzle exit relative to the surface of the impingement plate to be varied. The stagnation pressure and stagnation temperature of the nozzle were recorded on a 100 Hz facility DAQ for each test run.

The impingement plate consisted of an instrumented inner plate and an annular outer plate. The diameter of the impingement plate assembly was approximately sixty-six times that of the nozzle exit diameter. The instrumented plate had an array of holes that housed tube lines, which were connected to low-frequency (LF) pressure transducers located outside of the vacuum chamber and sampled by the 100 Hz facility DAQ. Several high-frequency (HF) pressure transducers were flush-mounted to the impingement plate surface and were sampled by a high-speed DAQ operating at 200 kHz. Additional details on the impingement plate instrumentation can also be found in Rodrigues *et al.*[6]

The PLIF laser systems were primarily located in a room adjacent to the vacuum chamber. A tunable ultraviolet (UV) laser beam with a wavelength near 226 nm, pulse duration of 10 ns, and repetition-rate of 10 Hz was generated by the PLIF laser system. In addition to Ref. 6, further details of the PLIF laser system can be found in Ref. 10. The PLIF laser beam was brought into the vacuum chamber through a UV-transmissive viewport and was directed to the test article using dichroic mirrors that were installed on remote-controlled mirror mounts. An optics structure located within the vacuum chamber was used to support the mirrors and two lenses, which were used to form the laser beam into a 2D laser sheet. The laser sheet was aligned to pass through the centerline of the jet and electronically excite the nitric oxide present in the jet flow. A glass plate was used to direct ~1% of the laser sheet energy towards a diffuser plate, which was used for laser monitoring purposes.

Fluorescence resulting from the laser-induced electronic excitation of NO was captured by an intensified sCMOS camera that was located within a pressurized enclosure near the test article. The camera enclosure was held at atmospheric pressure and was used to isolate the camera electronics from the lower pressure ambient environment. The PLIF camera featured a 100-mm focal length *f*/2.8 UV camera lens, with the field-of-view centered near the nozzle in the horizontal direction and allowed the entire vertical plume to be visualized for the range of nozzle altitudes tested. The secondary camera, located within a separate camera enclosure, monitored the laser sheet using blue fluorescence from the glass diffuser plate. The secondary camera was coupled with a 25-mm focal length *f*/1.4 visible camera lens. Additional details on the camera systems can also be found in Rodrigues *et al.*[6].

A summary of test conditions for the work discussed in this paper is provided in Table 1. Two different nozzle steady-state mass flow rates of approximately 8.1 g/s and 0.32 g/s are considered, which correspond to steady-state jet stagnation pressures of about $P_0 = 9.7 \cdot 10^5$ Pa and $P_0 = 3.8 \cdot 10^4$ Pa, respectively. The jet stagnation temperature was fixed at approximately $T_0 = 500$ K for all test cases. For each test, the ambient pressure in the vacuum chamber was set to near 600 Pa prior to opening the valve; the ambient pressure increased over the duration of the run primarily due to the jet flow issuing into the chamber. For the high-flowrate case of 8.1 g/s, six different nozzle altitudes, made dimensionless by the nozzle exit diameter, were considered: $h/D_e = 10$, 8, 5, 4, 3, and 2. At the $P_0 = 9.7 \cdot 10^5$ Pa stagnation pressure and Martian-relevant vacuum chamber pressure, the nozzle was operating in the underexpanded flow regime. Measurements were performed at two different nozzle altitudes, $h/D_e = 10$ and 3, for the low-flowrate case of 0.32 g/s. For this stagnation pressure of $P_0 = 3.8 \cdot 10^4$ Pa and at the Martian-relevant vacuum chamber pressure condition, the nozzle was operating in the overexpanded regime. Additional details regarding the underexpanded and overexpanded flow regimes for this nozzle can be found in Rodrigues *et al.*[6]

Table 1. Summary of test conditions.

$\dot{m}$ [g/s]	P_0 [Pa]	T_0 [K]	P_a [Pa]	h/D_e [-]
8.1	$9.68 \cdot 10^5$	504	605 – 641	10
	$9.67 \cdot 10^5$	504	599 – 635	8
	$9.64 \cdot 10^5$	505	598 – 640	5
	$9.64 \cdot 10^5$	503	602 – 638	4
	$9.67 \cdot 10^5$	501	597 – 635	3
	$9.65 \cdot 10^5$	503	601 – 639	2
0.32	$3.80 \cdot 10^4$	502	586 – 604	10
	$3.83 \cdot 10^4$	503	586 – 602	3

III. Results and Discussion

A. Underexpanded Jet

Representative instantaneous PLIF flow visualization for the underexpanded jet condition corresponding to $\dot{m}$ = 8.1 g/s is shown in Fig. 2 for six different dimensionless altitudes of h/D_e = 10, 8, 5, 4, 3, and 2. For the h/D_e = 10 image shown in Fig. 2(a), a well-defined barrel shape, normal shock (Mach disk), and unsteady shear layers are observed. The jet flow out of the nozzle appears to be steady, while unsteady flow features develop at the jet boundary downstream of the nozzle exit due to instabilities at the interface of the jet and the ambient quiescent environment. The jet core structure and a flow feature that is referred to here as the nozzle reflection point are also apparent downstream of the nozzle exit. For dimensionless altitudes corresponding to h/D_e = 8, 5, 4, 3, and 2, shown in Figs. 2(b) to 2(f), the well-defined barrel shape, steady jet flow out of the nozzle, and jet core feature are all similar to the h/D_e = 10 altitude. Another flow feature referred to here as the wall-jet is also clearly visible for all six h/D_e dimensionless altitudes. One interesting observation from the PLIF image in Fig. 2(a) for h/D_e = 10 is that a Mach disk but not a stagnation shock forms for this test condition, which is in stark contrast to the other h/D_e altitudes. At these other altitudes, a triangular-like surface shock rather than a Mach disk is apparent. The triangular-like surface shock appears to be an oblique shock that extends from the edge of the jet core to the jet shear layer. Furthermore, the height of the stagnation shock appears to be a strong function of h/D_e.

Time-averaged PLIF images for the underexpanded jet condition at h/D_e = 10, 8, 5, 4, 3, and 2 are shown in Fig. 3. The time-averaged images were computed using a sample size of 100 images acquired during the steady-state portion of the run. While the unsteady features appear to be smoothed-over for the time-averaged images, relatively steady features such as the jet core, jet edge, and stagnation shock are more clearly visible. The time-averaged spatial shape of the wall-jet is also revealed in these images, as a lifted wall-jet can be seen a few jet diameters away from the centerline at all six h/D_e altitudes. The lifted wall-jet is perhaps most pronounced at the lower h/D_e altitudes, such as h/D_e = 3 in Fig. 3(e) and h/D_e = 2 in Fig. 3(f). It should be noted that the lifted wall-jet was also observed in the experiments performed by Inman *et al.*[8]

Evidence of the lifted wall-jet is also apparent in the measured spatial distribution of impingement pressure. Time-averaged measurements using the low-frequency pressure transducers at several different locations relative to the nozzle centerline are shown in Fig. 4 as a function of the dimensionless axis x'/D_e. The notation x' is used to denote a corrected position for the nozzle centerline with respect to the center of the impingement plate and is the same convention used in the test overview reported in Ref. 6. Also shown in Fig. 4 is a curve-fit based on local polynomial regression using the LOESS (locally estimated scatterplot smoothing) method, after assuming an axisymmetric pressure distribution with respect to the jet centerline. It is apparent that a low-pressure (suction) region where the local plate pressure is below the ambient pressure exists for all six h/D_e conditions. The exact location of this low-pressure region appears to slightly vary with h/D_e. As observed in Rodrigues *et al.*[6], the structure of the impingement pressure distribution for this experiment is similar to the reported observation for the experiment by Inman *et al.*[8]. The impingement pressure distribution at h/D_e = 8, 5, and 4 also reveals a double-peak structure, with the peaks occurring near $x'/D_e = \pm 2$. This double-peaked spatial structure in the pressure distribution was also observed by Inman *et al.*[8] The higher impingement pressures away from the jet centerline can be attributed to the high-velocity jet boundary impinging on the flat plate. Unfortunately, a similar conclusion regarding the pressure distribution cannot be drawn for this jet condition at h/D_e = 10, 3, and 2, as four pressure transducers near the center of the plate over-ranged. However, we can conclude that for this jet condition, a plate pressure exceeding $2.7 \cdot 10^3$ Pa (20 Torr) is present.

The measured plate pressure at x'/D_e = 1.4 (the point closest to the centerline containing data for all runs) as a function of the dimensionless altitude h/D_e is shown in Fig. 5. Also shown in Fig. 5 are the time-averaged PLIF images for the different h/D_e considered, which provide context to the pressure measurement. At first glance, it is puzzling that the impingement pressure at h/D_e = 10 is significantly greater than the impingement pressure at h/D_e = 8. However, this can be explained using the PLIF visualization, as the normal shock for h/D_e = 10 results in a greater post-shock static pressure compared to the apparent oblique shock for h/D_e = 8. A further decrease in h/D_e from 8 to 2 results in a continuous increase in the impingement pressure.

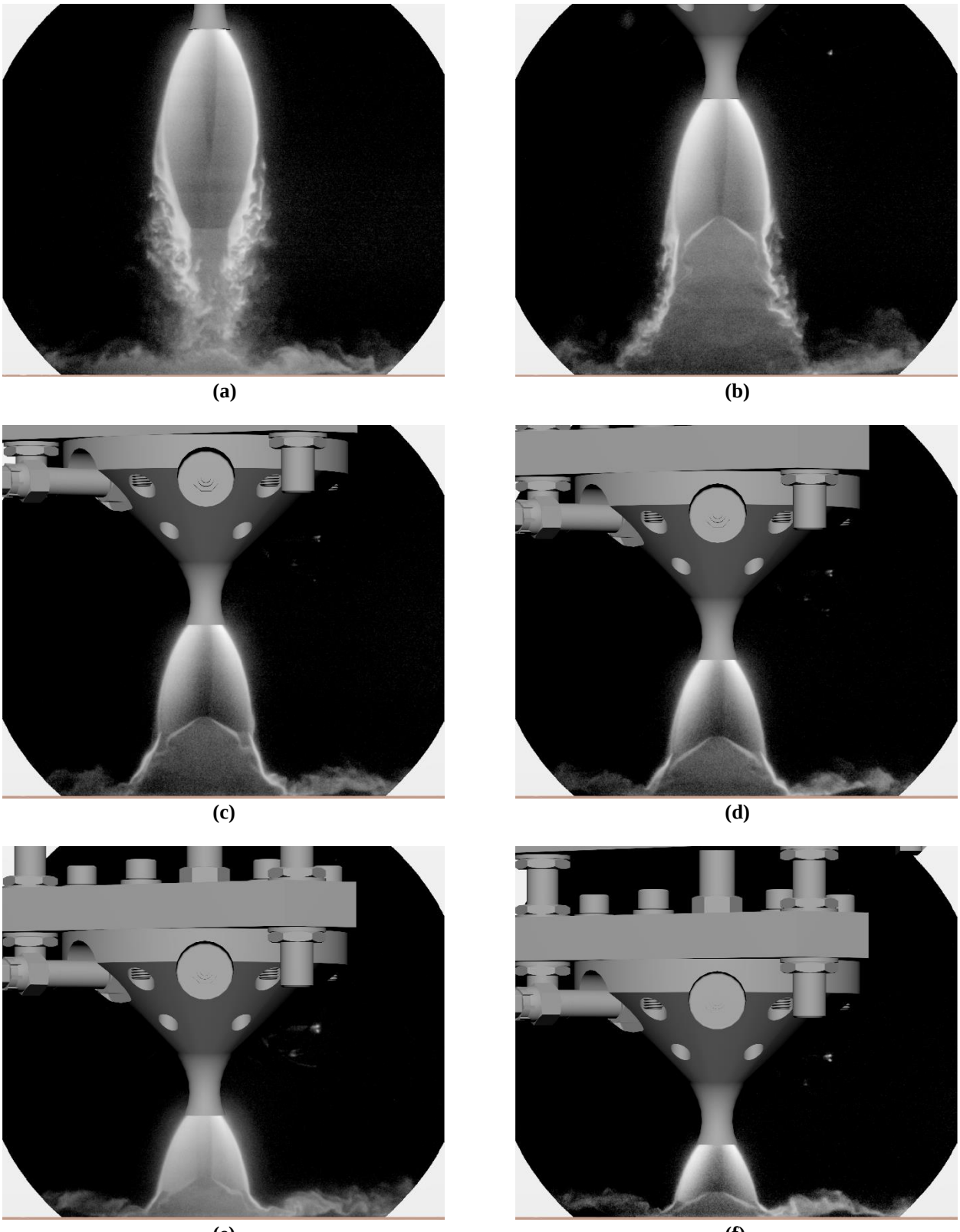

Fig. 2 Representative instantaneous PLIF images at six different h/D_e for the underexpanded flow condition: (a) h/D_e = 10, (b) h/D_e = 8, (c) h/D_e = 5, (d) h/D_e = 4, (e) h/D_e = 3, and (f) h/D_e = 2.

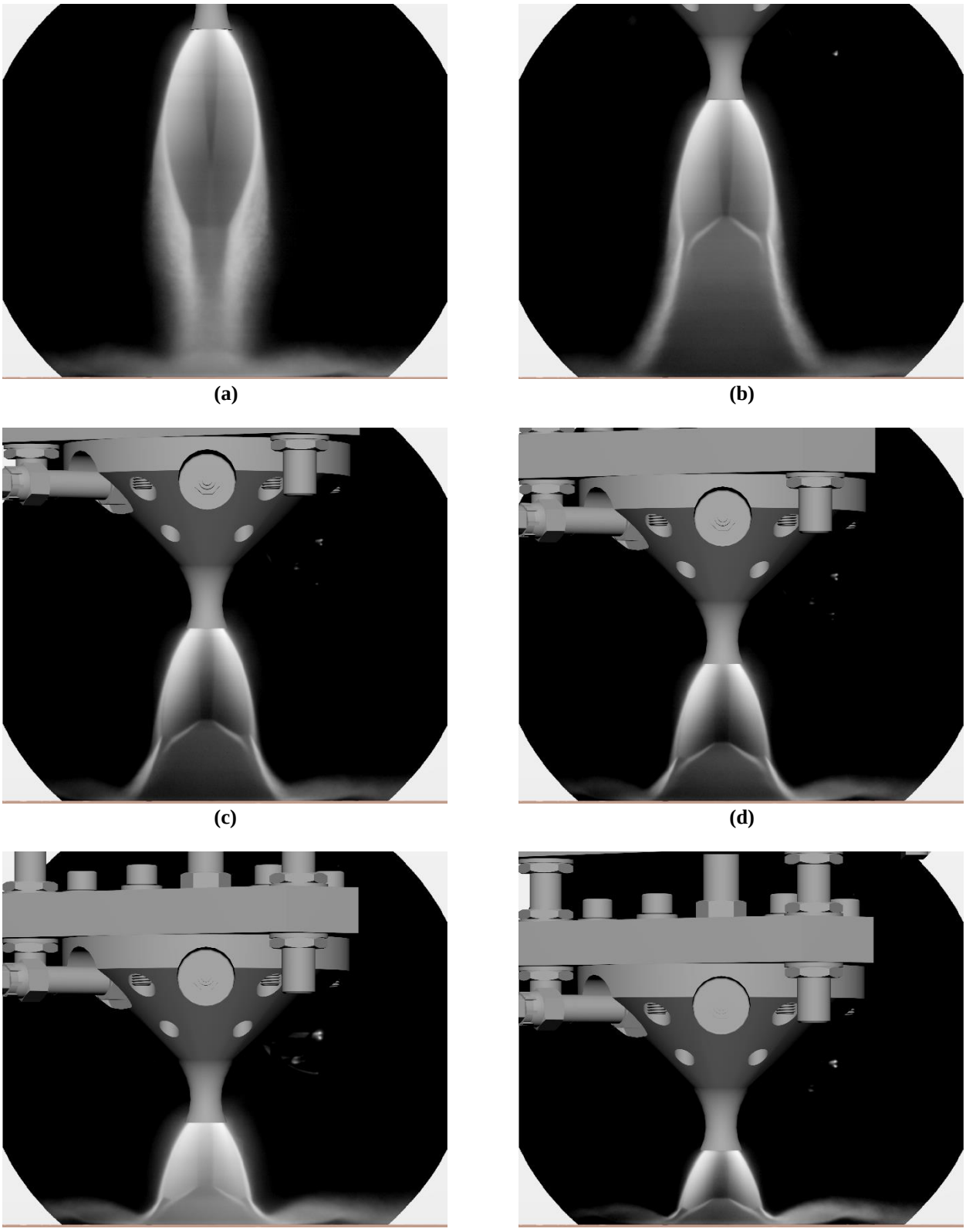

(a) **(b)**

(c) **(d)**

(e) **(f)**

Fig. 3 Time-averaged PLIF images at six different h/D_e for the underexpanded flow condition: (a) h/D_e = 10, (b) h/D_e = 8, (c) h/D_e = 5, (d) h/D_e = 4, (e) h/D_e = 3, and (f) h/D_e = 2.

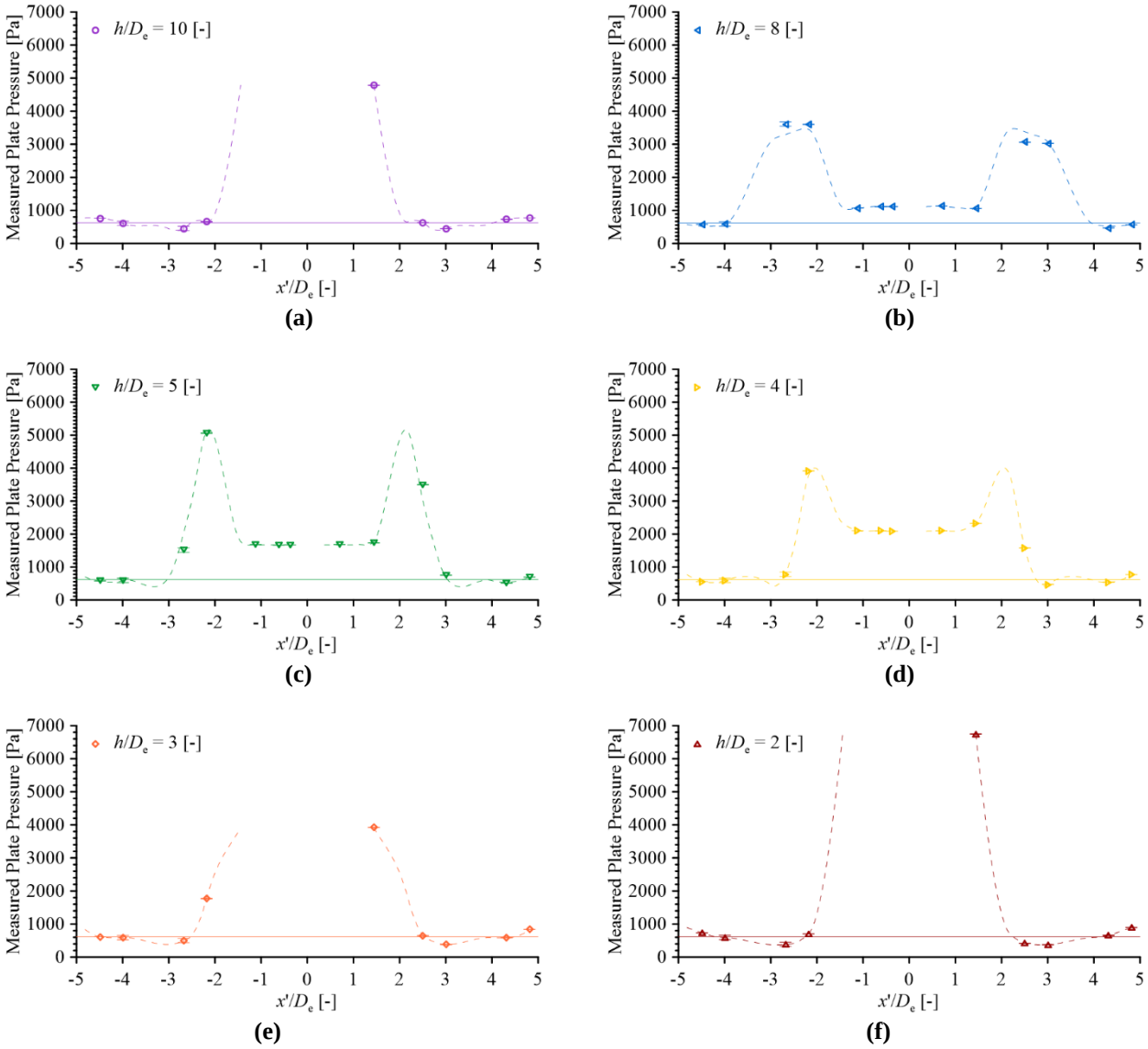

Fig. 4 Time-averaged measured plate pressure vs. x'/D_e at six different h/D_e for the underexpanded flow condition: (a) h/D_e = 10, (b) h/D_e = 8, (c) h/D_e = 5, (d) h/D_e = 4, (e) h/D_e = 3, and (f) h/D_e = 2.

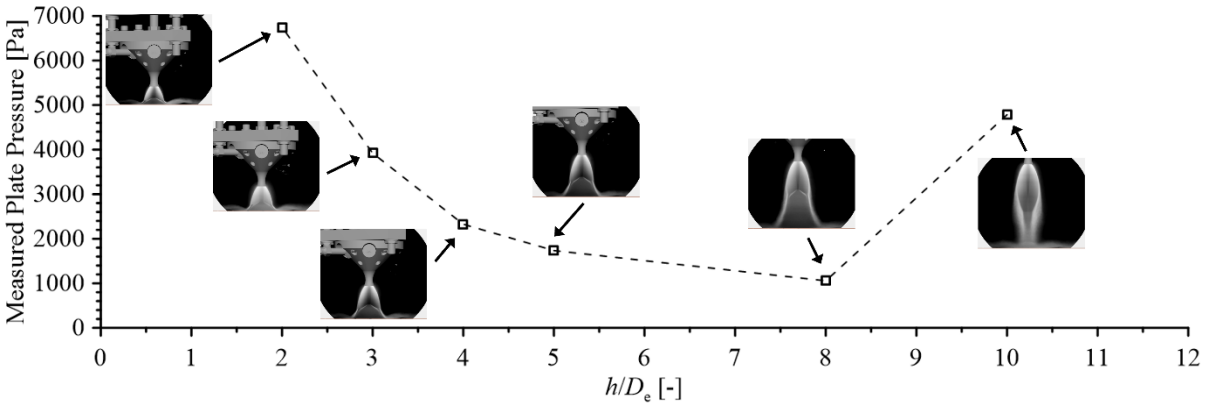

Fig. 5 Time-averaged measured plate pressure vs. dimensionless altitude h/D_e for the underexpanded flow condition at a location corresponding to x'/D_e = 1.4.

B. Overexpanded Jet

Representative instantaneous PLIF flow visualization for the overexpanded jet condition corresponding to $\dot{m}$ = 0.32 g/s is shown in Fig. 6 for two dimensionless altitudes of h/D_e = 10 and h/D_e = 3. At this condition, the nozzle appears to operate in the overexpanded regime with significant flow separation upstream of the nozzle exit. A highly collimated, laminar, unsteady jet is observed at h/D_e = 10 and no significant impingement plate effects appear to be present. While a highly collimated, laminar, unsteady jet is also observed at h/D_e = 3, a *tree-trunk* like structure can be observed at the impingement plate near the jet centerline. The jet appears to transition from steady to unsteady several diameters downstream of the nozzle at h/D_e = 10. Whereas for the h/D_e = 3 case, the flow appears to be primarily unsteady from approximately one diameter downstream of the nozzle to the impingement region.

The time-averaged PLIF images shown in Fig. 7 also provide insights on the flow separation. A significant density gradient appears to be present near the nozzle exit based on the contrast of the PLIF signal intensity, which may potentially be a normal shock due to the significant flow separation. The time-averaged impingement pressure distribution in Fig. 8 shows a similar double-peaked structure for the overexpanded jet as select conditions of the underexpanded jet, which can also be attributed to the high velocity jet boundary impinging on the flat plate. However,

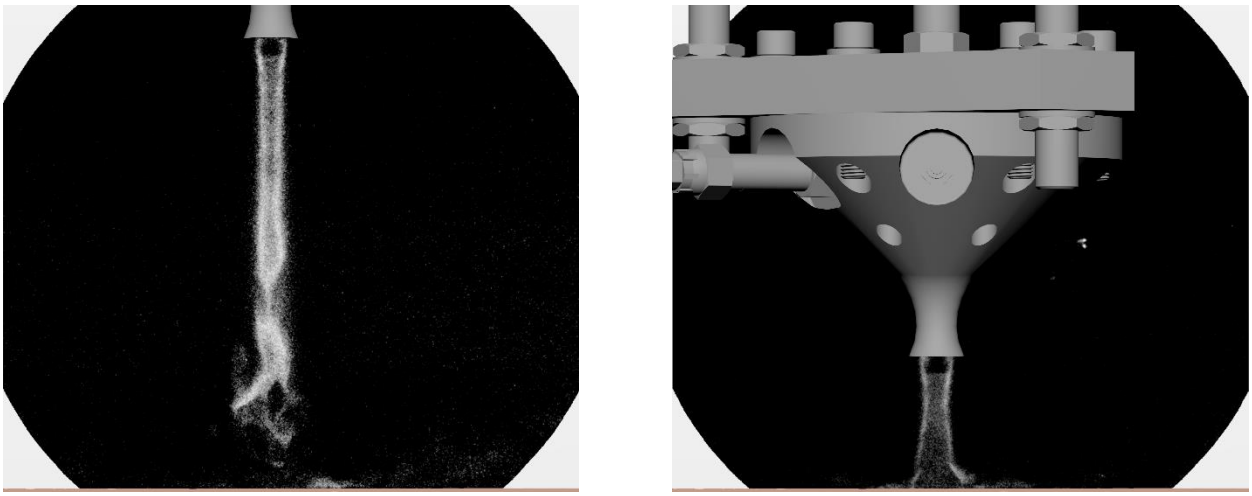

(a) **(b)**

Fig. 6 Representative instantaneous PLIF images at two different h/D_e for the overexpanded flow condition: (a) h/D_e = 10 and (b) h/D_e = 3.

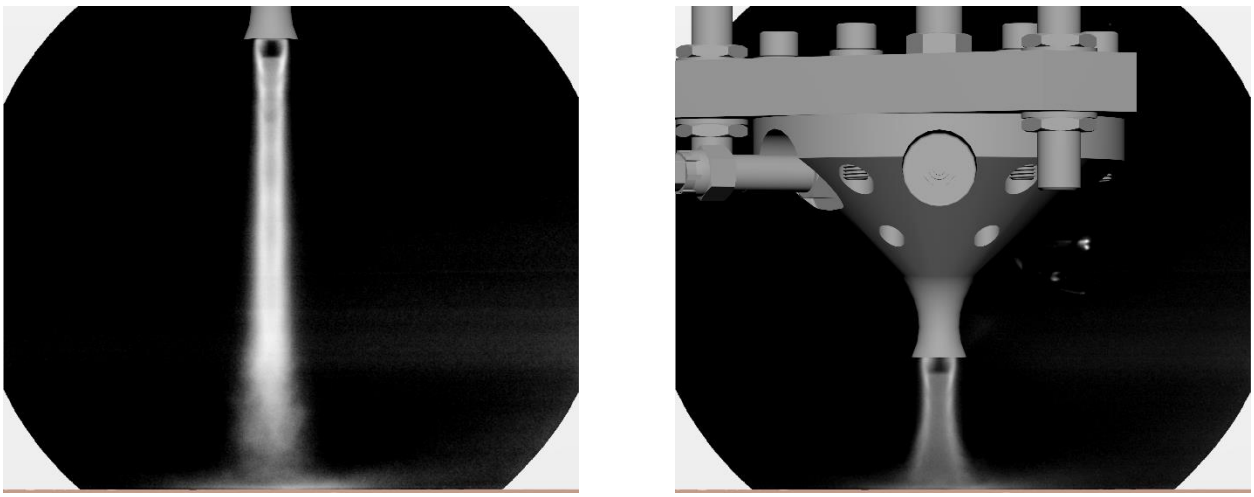

(a) **(b)**

Fig. 7 Time-averaged PLIF images at two different h/D_e for the overexpanded flow condition: (a) h/D_e = 10 and (b) h/D_e = 3.

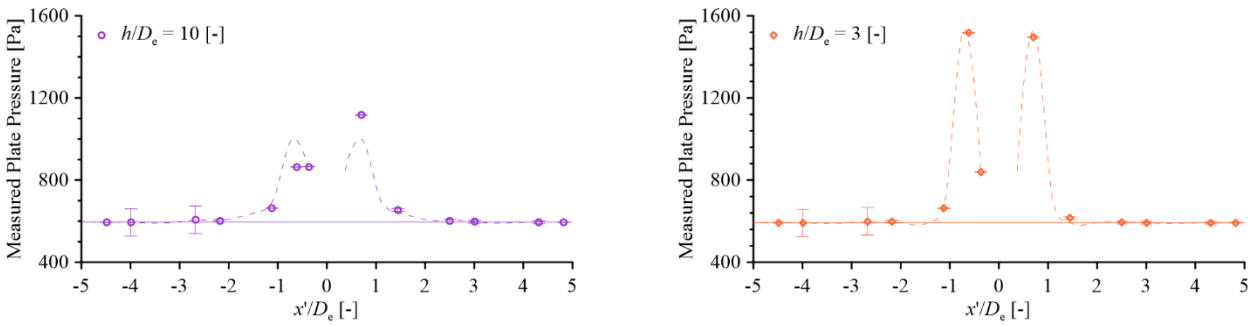

Fig. 8 Time-averaged measured plate pressure vs. x'/D_e at two different h/D_e for the overexpanded flow condition: (a) h/D_e = 10 and (b) h/D_e = 3.

the location of the peaks appear to be near $x'/D_e = \pm 0.5$ for the overexpanded case, approximately coinciding with the extent of the jet boundary of the highly collimated jet. Neither a lifted wall-jet nor a low-pressure (suction) region for the pressure distribution appear to be present at these conditions.

IV. Summary and Conclusions

In the present work, we report flow visualization for plume-surface interaction at Martian-relevant ambient pressure conditions. Measurements were performed on a supersonic flow impinging on a flat plate within a large-scale vacuum chamber environment. Two different mass flow rate conditions, corresponding to an underexpanded jet and an overexpanded jet, were investigated and measurements were acquired at six different nozzle heights relative to the impingement surface. Representative instantaneous and time-averaged visualizations of the two jet flows are presented using planar laser-induced fluorescence (PLIF), along with the time-averaged measured spatial distribution of impingement pressure. Significant differences in the stagnation shock structure based on the dimensionless altitudes are observed for the underexpanded jet, which help explain the unexpected behavior in the impingement pressure. Significant flow separation at the nozzle exit for the overexpanded jet are also revealed by the PLIF visualization.

Acknowledgments

The authors wish to acknowledge the support of the *Plume Surface Interaction* project, which was funded by the NASA Space Technology Mission Directorate (STMD) Game Changing Development (GCD) program with S. Harris from NASA Marshall Space Flight Center (MSFC) serving as project manager. The authors also thank Dr. Manish Mehta for setting the initial direction of this work. The authors also wish to acknowledge the technical input on test design and direction from Dr. Jeff West, Dr. Andrew Weaver, and Thomas Shurtz from MSFC. The measurements reported in this paper were part of a larger ground test campaign and several people from MSFC are acknowledged for these efforts, including Tracy Reynolds, Tom Liu, Jeffrey Rayburn, Howard Soohoo, Kevin Thompson, Dr. Jim Sisco, Kristian Miasek, and Kevin Baker. Finally, the authors also thank W. Holt Ripley from the NASA Langley Research Center for assistance with preparation and shipment of PLIF equipment to the test facility, J. Sebastian Rubio from the Johns Hopkins University for assistance with the PLIF set-up in the vacuum chamber, and Dr. Timothy Fahringer for assistance with the spatial calibration of the PLIF images.

References

[1] Korzun, A. M., Eberhart, C. J., West, J., Liever, P., Weaver, A., Mantovani, J., Langton, A., Kemmerer, B., and Atkins, A. "Design of a Subscale, Inert Gas Test for Plume-Surface Interactions in a Reduced Pressure Environment," AIAA 2022-1808. *AIAA SCITECH 2022 Forum*. January 2022.

[2] Eberhart, C. J., West, J., and Korzun, A. M. "Overview of Plume-Surface Interaction Data from Subscale Inert Gas Testing at NASA MSFC Test Stand 300 Vacuum Facilities," AIAA 2022-1810. *AIAA SCITECH 2022 Forum*. January 2022.

[3] Diaz-Lopez, M. X., Gorman, M., Rubio, J. S., and Ni, R. "Plume-surface Interaction Physics Focused Ground Test 1: Diagnostics and Preliminary Results," AIAA 2022-1809. AIAA SCITECH 2022 Forum. January 2022.

[4] Rubio, J. S., Gorman, M., Diaz-Lopez, M. X., and Ni, R. "Plume-Surface Interaction Physics Focused Ground Test 1: Setup and Preliminary Results," AIAA 2022-1809. AIAA SCITECH 2022 Forum. January 2022.

[5] Danehy, P. M., Weisberger, J., Johansen C., Resse, D., Fahringer, T., Parziale, N. J., Dedic C., Estevadeordal, J., and Cruden, B. A., "Non-Intrusive Measurement Techniques for Flow Characterization of Hypersonic Wind Tunnels," NATO STO Manuscript on Hypersonic Freestream Characterization, 2018.

[6] Rodrigues, N. S., Tyrrell, O. K., Danehy, P. M., Eberhart, C. J., McDougal, K. J., Liu, T., Reynolds, T. D., Rubio, J. S., Jiang, N., Hsu, P., and Korzun, A. M. "Flow Visualization for Plume-Surface Interaction Testing Within Large-Scale Vacuum Environments at Conditions Relevant to Lunar and Martian Landers", JANNAF Exhaust Plume and Signatures Annual Meeting. December 2023.

[7] Tyrrell, O. K., Rodrigues, N. S., Korzun, A. M., and Danehy, P. M. "Flow visualization of intrusive and non-intrusive configurations for lunar- and Martian-relevant plume-surface interaction," AIAA 2024-2499. AIAA SCITECH 2024 Forum. January 2022.

[8] Inman, J. A., Danehy, P. M., Nowak, R. J., and Alderfer, D. W., "Fluorescence imaging study of impinging underexpanded jets," AIAA 2008-619. 46th AIAA Aerospace Sciences Meeting and Exhibit. January 2008.

[9] Inman, J. A., Danehy, P. M., Nowak, R. J., and Alderfer, D. W., "The Effect of Impingement on Transitional Behavior in Underexpanded Jets," AIAA 2009-591. 47th AIAA Aerospace Sciences Meeting and Exhibit. January 2009.

[10] Rodrigues, N. S., Bathel, B., Danehy, P. M. "A Comparison of NO Laser-induced Fluorescence Models at conditions relevant to Supersonic and Hypersonic Flows", AIAA 2022-0897. *AIAA SCITECH 2022 Forum*. January 2022.